Imaging and quantifying salt tracer transport in a riparian groundwater system by means of 3D ERT monitoring

[1,2]Joseph Doetsch (jdoetsch@lbl.gov), [3]Niklas Linde (Niklas.Linde@unil.ch),

[4,5]Tobias Vogt (Tobias.Vogt@nagra.ch), [6]Andrew Binley (a.binley@lancaster.ac.uk),

[1]Alan G. Green (green@aug.ig.erdw.ethz.ch)

[1] Institute of Geophysics, ETH Zurich, Zurich, Switzerland

[2] Earth Sciences Division, Lawrence Berkeley National Laboratory, Berkeley, CA

[3] Institute of Geophysics, University of Lausanne, Lausanne, Switzerland

[4] Eawag – Swiss Federal Institute of Aquatic Science and Technology, Dübendorf, Switzerland

[5] NAGRA, Wettingen, Switzerland

[6] Lancaster Environment Centre, Lancaster University, Lancaster, U.K.

Running Head: 3D ERT monitoring of salt tracer transport

Intended for publication in *Geophysics*

ABSTRACT

Determining groundwater flowpaths of infiltrated river water is necessary for studying biochemical processes in the riparian zone, but their characterization is complicated by strong temporal and spatial heterogeneity. Here, we investigate to what extent repeat 3D surface electrical resistance tomography (ERT) can be used to monitor transport of a salt tracer plume under close to natural gradient conditions. The aim is to estimate groundwater flow velocities and pathways at a site located within a riparian groundwater system adjacent to the peri-alpine Thur River in northeastern Switzerland. Our ERT time-lapse images provide constraints on the plume's shape, flow direction, and velocity. These images allow the movement of the plume to be followed for 35 m. Although the hydraulic gradient is only 1.43‰, the ERT time-lapse images demonstrate that the plume's center of mass and its front propagate with velocities of 2×10^{-4} m/s and 5×10^{-4} m/s, respectively. These velocities are compatible with groundwater resistivity monitoring data in two observation wells 5 m from the injection well. Five additional sensors in the 5 - 30 m distance range did not detect the plume. Comparison of the ERT time-lapse images with a groundwater transport model and time-lapse inversions of synthetic ERT data indicate that the movement of the plume can be described for the first 6 h after injection by a uniform transport model. Subsurface heterogeneity causes a change of the plume's direction and velocity at later times. Our results demonstrate the effectiveness of using time-lapse 3D surface ERT to monitor flow pathways in a challenging peri-alpine environment over larger scales than what is practically possible with crosshole 3D ERT.

INTRODUCTION

Riparian (river margin) groundwater dynamics are distinguished by temporal and spatial variations of flux exchanges between rivers and groundwater over a wide range of scales (Woessner, 2000). Temporal variations are caused by changing hydrological conditions, such as increasing or decreasing river level (Keery et al., 2007; Vogt et al., 2010b). Spatial variations result from riverbed morphology and curvature, as well as spatially varying hydraulic conductivities (Storey et al., 2003; Cardenas et al., 2004). The hydraulic conductivities of fluvial sediments typically range over several orders of magnitude (Heinz et al., 2003; Bayer et al., 2011), with the nature of the depositional structures determining the distribution of hydraulic conductivities (Renard and de Marsily, 1997; Kerrou et al., 2008).

Reliable information on subsurface flow velocities and pathways is needed for quantitative groundwater studies in riparian environments. For reactive transport, it is also necessary to determine solute residence times for estimating exchanges, losses, and gains along flow pathways. The impact of solute transport on biogeochemical processes in the hyporheic (mixing zone between ground- and surface water) and riparian zones is well recognized (Bencala, 1984; Stanford and Ward, 1988). Consequently, having trustworthy information on groundwater flow paths allows groundwater sampling for investigating biogeochemical processes in the hyporheic and riparian zones to be optimally located.

Hydraulic head measurements alone are often insufficient for characterizing flow pathways in very permeable environments because of large measurement uncertainties with respect to the typically small head gradients and the inherent depth averaging of such data. Solute tracer tests offer means to infer pathways through multi-well sampling, but the significant number of sampling wells needed to outline tracer plumes under natural flow conditions make such approaches excessively invasive and expensive, and there is a risk that the tracer bypasses monitoring wells (Boggs and Adams, 1992). Although natural fluctuations of such physical

variables as temperature and electrical resistivity of water (Hoehn and Cirpka, 2006; Cirpka et al., 2007; Constantz, 2008; Vogt et al., 2010a) provide the possibility of quantifying river - groundwater interactions via their traveltimes, the flow directions and velocities are usually not well determined. Geophysical monitoring of tracer movement can be a useful complement to conventional tracer experiments, offering larger scale integrated measurements of solute concentration in a minimally invasive manner (Ward et al., 2010). The results from such measurements may help target more direct conventional sampling.

Common geophysical techniques for monitoring solute transport in groundwater systems are single-hole and crosshole ground-penetrating radar (GPR) (e.g., Ramirez and Lytle, 1986; Day-Lewis et al., 2003; Dorn et al., 2011) and surface and crosshole electrical resistance tomography (ERT) (e.g., Slater et al., 2000; Binley et al., 2002; Kemna et al., 2002; Singha and Gorelick, 2005; Cassiani et al., 2006). While having limited depth resolution, surface ERT monitoring has the advantage of being largely automated and minimally intrusive, because electrodes only penetrate ~20 cm below the surface and thus have insignificant influence on groundwater flow. Although the influence of boreholes, needed for hydrological measurements and crosshole surveys, on groundwater flow is often neglected, vertical flow through open or screened wells can have important effects in highly heterogeneous or stratified media (Butler et al., 2009).

Geophysical monitoring of salt tracer tests using ERT has been successful in the laboratory (Slater et al., 2000) and in the field using 2D and 3D crosshole techniques (Singha and Gorelick, 2005; Wilkinson et al., 2010). Studies in which a salt tracer has been monitored from the surface have so far mainly been restricted to measurements along single or several 2D lines (Cassiani et al., 2006; Monego et al., 2010; Ward et al., 2010; Cardenas and Markowski, 2011). An early example of surface based 3D plume monitoring is Park (1998), who investigated a water tracer in the vadose (unsaturated) zone. The value of 2D surveys are limited not only in terms of spatial coverage, but also because 2D inversions provide models that explain data associated with 3D

4

targets with equivalent 2.5D models, which inevitably create biased models that make quantitative investigations more difficult. Measurements over time on a 2D surface grid and inversion in 3D do not suffer from this latter limitation.

In this contribution, we describe a 3D surface ERT monitoring study in which inversions of geophysical data provided answers to some seemingly basic questions about flow patterns. The novelty of this study relates primarily to the added value offered by 3D surface ERT monitoring to solve an important field-based hydrological problem under natural, highly advective flow conditions. At this study site, rather extensive hydrological tests involving numerous wells failed to provide reliable information about flow direction, velocity and flow paths. Our experiment involved injecting a salt tracer into a gravel aquifer through an injection well and then monitoring the evolution of the tracer plume using surface ERT and continuous measurements of hydraulic head and water electrical resistivity in a number of observation wells. The measurements were carried out on a gravelbar overlying a highly permeable groundwater system in direct contact with a restored stretch of the Thur River, northeastern Switzerland. At this site, transects of wells extending from the river in the direction of expected groundwater flow have been established. A multidisciplinary group of researchers has been using these wells to study biochemical reactions and transport of micro-pollutants as a function of residence times and distances from the river under the assumption that sampling takes place along a flow line. A first well transect was defined at an angle of 45° from the river on the basis of available head data from specifically installed observation wells (see Schneider et al. (2011) for details), but it was impossible to recover any mass after tracer tests despite rather intense pumping in the observation well. The well transect was then refined to an angle of 30° from the river on the basis of a more extensive set of head data, but the mass recovery after tracer tests was extremely low. The ERT results presented here provide a credible explanation for why the two transects were unsuitable for tracking the flowpath and

suggests that ERT monitoring of tracer tests should be performed prior to installing extensive well transects along supposed flow paths.

The time-lapse 3D geophysical models are here used to follow the tracer plume's center of mass and provide some insights about the tracer front and tail. The velocity of the plume's center of mass is determined from its movement history, which allows us to construct a best-fitting homogeneous flow and transport model that explains the ERT-estimated center of mass movements at early times. Subsequently, we simulate the tracer experiment and convert the synthetic tracer concentrations into electrical resistivity perturbations and corresponding synthetic noise-contaminated ERT data. These data are then inverted using the same parameters as employed for the field data. By studying the different images obtained from the idealized plume behavior and observed response we are thus able to provide useful information on preferential flow and tailing for this specific experimental setup. In the following, we describe the field setup and ERT data processing and inversion before introducing the hydrological modeling.

THUR RIVER FIELD SITE

Our target area is an alluvial aquifer adjacent to the Thur River in northeastern Switzerland (see inset in Figure 1). This river was channelized at the end of the 19th century. Starting in 2000, a more natural environment was restored along a 2.5 km stretch of the river. The effects of restoration at the Thur River have been investigated in a large multidisciplinary research initiative (RECORD, 2011); instrumentation and characteristics of the study site are described by Schneider et al. (2011).

Most research is concentrated across the restored riparian zone on the northern side of the river and in an adjacent woodland, within which numerous 5-cm-diameter observation wells have been instrumented (Figure 1). Well cores and surface and crosshole geophysical surveys delineate a 5-6 m thick sandy gravel aquifer. In the riparian zone outside of the active river channel, a silty

fine-sand layer of variable thickness (0-3 m) overlies the aquifer. Underlying the aquifer is a clay-rich aquitard. Extensive 3D surface ERT and GPR measurements have been made from the region of the tracer injection well (Figure 1b) to ~240 m downstream (Doetsch et al., 2012). Figure 2a displays a vertical slice through the 3D GPR volume that delineates the base of the aquifer. The gravel - clay boundary has been mapped beneath the entire GPR survey area. Figure 2b shows a portion of the ERT model.

The river is well connected to the groundwater system, such that river-level fluctuations produce near instantaneous changes to the groundwater table; the main groundwater recharge at the study site originates from continuous river water infiltration. Seepage velocities in the river bed vary locally between 1.5 and 4.0×10^{-5} m/s (Vogt et al., 2010b), and groundwater flow velocities in the riparian zone are estimated to be $\sim 10^{-4}$ m/s (Vogt et al., 2010a). According to multi-level slug tests (local test of hydraulic conductivity) in fully screened wells, the hydraulic conductivity of the aquifer has a geometric mean of 3.1×10^{-3} m/s (Schneider et al., 2011).

SALT TRACER EXPERIMENT

Salt tracer injection

Many of the ongoing and planned hydrogeological and biogeochemical studies at the Thur site (Schneider et al., 2011) have been based on the erroneous assumption that the groundwater samples have been taken along a well transect that approximately followed the groundwater flow direction. Attempts to constrain groundwater velocity and flow direction from previous tracer tests failed because the tracer was not observed in any monitoring wells during the natural gradient tests and recovery rates were very small even during the forced gradient experiments. The salt tracer injection and ERT monitoring described here were carried out to determine the actual flow direction and velocity in the vicinity of the well transect.

For monitoring the salt tracer, we installed sensors with integrated data loggers (hydraulic head, water temperature, and water electrical resistivity) in the river and at 365.9 – 367.5 m elevation (4.2 – 5.8 m below the groundwater table) in the six observation wells shown in Figure 1. In observation well R073, an additional sensor was installed at ~370.4 m elevation (1.3 m below the groundwater table). Since the main purpose of the tracer test was to determine natural groundwater flow directions and velocities, there was no pumping in the observation wells. The injection well R042 (see Figure 1b) was located ~5 m from the main river channel and ~15 m from the edge of the river at the time of the tracer test. The local hydraulic conductivity around the tracer injection well (R042) as inferred from multi-level slug tests was $5.8 \pm 2.9 \times 10^{-3}$ m/s, with the highest values in the middle and the lowest values at the bottom of the aquifer. We defined our coordinate system with the origin at the injection well R042 (SwissGrid coordinates 700467.86 / 271981.94) and the *x*-axis in the expected flow direction at an azimuth of 315°.

Measurements in the injection well and six observation wells just before tracer injection were used to estimate the hydraulic head field with respect to the injection well (Figure 1a). The hydraulic head gradient inferred from these measurements was 1.43‰ in a direction subparallel to the river. The Thur River, which usually has strongly varying discharge and stage, was very stable during the ERT monitoring experiment (11 – 13 October 2010); Figure 3a demonstrates that water-level fluctuations during the entire monitoring experiment were minor. For the 16 h period that we used for comparison with the groundwater model (gray shaded area in Figure 3a), the variation in river-water level was only ±2 cm. Hydraulic head time series in the observation wells revealed that hydraulic head fluctuations were even smaller: only ±1 cm. These fluctuations caused variations in hydraulic head gradient of ±4° in direction and ±0.07‰ in magnitude during the tracer experiment. Twenty hours of ERT monitoring prior to the tracer injection showed that hydraulic head variations on this order had no significant effect on the geophysical data.

The electrical resistivity of the river water was also very stable (±1%) throughout the experiment (Figure 3b) and temperature variations in the monitoring boreholes were only ±0.1° C (i.e., below the specified error level of the temperature sensors) during the same period. The effect of subsurface temperature variations on electrical conductivities (Waxman and Thomas, 1974) could therefore be safely neglected.

A total of 500 l of saline water containing 18 kg of dissolved NaCl (36 g/l concentration with electrical resistivity ρ_w of ~0.17 Ωm or electrical conductivity σ_w of ~60 mS/cm) was injected into well R042 for 20 min (pumping rate 0.4 l/s) starting at 15:33 on 11 October 2010. During and immediately after injection, the tracer was thoroughly mixed over the entire fully penetrating screen from 0.5 to 6 m below the water table. It is clear that the increased pressure during the injection phase will initially distribute the tracer in a radial fashion around the injection well, but the flow will return to the natural conditions very quickly after the end of injection. The increase in hydraulic head during the injection could not be directly measured, but the hydraulic head within the injection well had returned to the pre-injection level when monitoring was resumed a few minutes after the end of injection. Hydraulic head time series in the observation wells showed no disturbances that could be related to the tracer injection.

Salt tracer breakthrough

Only two of the sensors downgradient of the injection well detect electrical-resistivity changes in the groundwater that could be attributed to tracer arrival (Figure 4). These 4.8-m-depth sensors in observation wells R072 and R073 are both located ~5 m from the injection well (Figure 1b). The resistivity time series are converted to salt concentrations via a laboratory-determined linear relationship based on concentrations and resistivities spanning the full concentration range expected in the field. Using Equation 13 of Kemna et al. (2002), we estimate the constant of proportionality of this relationship to be $\gamma = 0.53$ (g/l)/(mS/cm). The tracer breakthrough curves in

Figure 4 demonstrate that the sensor in observation well R072 registers the first arrival of the tracer only 50 min after salt injection began. The peak concentration of 4.8 g/l (i.e., 13% of the injection concentration) is observed at 14.4 h. The breakthrough curve has a long tail with a significant amount of salt present after 140 h (5 days). The resistivity sensor installed in observation well R073, only 2.6 m from R072, records tracer breakthrough much later and with much smaller concentrations, with the first arrival at ~20 h and a peak concentration of 0.8 g/l at ~88 h. A second resistivity sensor located 1.3 m below the groundwater table in observation well R073 does not detect any tracer, suggesting that the tracer moved primarily in the lower part of the aquifer. This effect is probably mainly due to the higher density of the injected tracer.

ERT DATA ACQUISITION, PROCESSING, AND INVERSION

Data acquisition

A total of 144 electrodes were deployed (Figure 1) for the full duration of the monitoring experiment. This layout was designed to image the plume close to the injection well and track its movement for ~30 m. It included 16 × 7 electrodes installed at a 4 × 6 m spacing. Electrode spacing was decreased to 2 m along the extended central line of the grid (Figure 1a). The axis of the electrode grid was oriented parallel to the anticipated groundwater flow direction and the x-axis. A Syscal Pro resistivity meter was used to record data provided by 3031 four-electrode arrays that comprised dipole-dipole, equatorial dipole-dipole, Wenner, and gradient configurations (Zonge et al., 2005). 3D coverage was ensured by measuring all configurations along the two perpendicular directions of the electrode grid.

ERT monitoring was initiated 20 h before tracer injection to determine the influence of natural variations on the data. These measurements showed that the repeatability of the measurements was very high. Natural variations within this period were <1% for more than 90% of the ERT configurations. Monitoring was stopped during the tracer injection and resumed once the tracer

had been injected. The data set acquired just before tracer injection was used as the baseline data for the time-lapse inversions. The acquisition time for each complete suite of 3031 measurements was ~45 min. We collected one data set per hour for the first 7 h hours and one data set approximately every 2.25 h thereafter. A total of 26 sets of data were recorded during ~50 h of post-injection recording. To quantify measurement errors, two complete reciprocal data sets were also collected, one directly before tracer injection and one at the end of the ERT monitoring. Previous monitoring experiments at the site and results from the pre-injection monitoring showed that the reciprocal errors are very small (median of 0.3%). To avoid long acquisition times that would decrease the temporal sampling, reciprocal measurements were therefore not acquired at each time-step.

Preprocessing the ERT data

An apparent resistivity time series of 27 values (baseline plus post-injection data) was constructed for each of the electrode configurations. After rejecting data with high geometrical factors (>5000 m) and data affected by poor electrode coupling and excessive noise levels, a total of 2461 ERT time series were available for further analysis. The static error ε_s associated with each configuration was determined from the two reciprocal data sets (median of 0.3%). An assumed baseline error of 3% was then added to the reciprocal errors as reciprocal error estimates do not incorporate important error sources, such as geometrical or modeling errors. These error estimates were used for the initial baseline ERT inversion using robust data reweighting (Claerbout and Muir, 1973), which adapts the estimated errors for data that do not agree well with the model predictions. The resulting error estimates used for the baseline ERT inversion had a median value of 3.8%.

For most ERT monitoring experiments, the 1 - 2 h required to record each suite of data is short compared to the movement of the tracer (on the order of days), thus justifying the common

assumption that significant changes do not occur during data acquisition (Binley et al., 2002; Kemna et al., 2002; Cassiani et al., 2006; Wilkinson et al., 2010). However, for experiments in fast dynamic environments, such as ours, the timing of each measurement has to be taken into account (Day-Lewis et al., 2003). To interpolate the ERT measurements to identical times for each electrode configuration, a spline algorithm was applied to each smoothly varying time series. This process effectively compensated for subsurface resistivity changes during the ~45 minute acquisition periods.

ERT mesh generation and determination of the baseline bulk resistivity model

Versatile finite-element ERT modeling and inversion codes (Günther et al., 2006; Blome et al., 2009) make it possible to include arbitrary geometries in the inversion mesh and to impose various constraints on the inversion process. An appropriate mesh and suitable regularization are crucial for both static and time-lapse ERT inversions. Unstructured (e.g., tetrahedral) finite-element meshes offer the possibility to incorporate surface topography and known subsurface structures. We used a tetrahedral mesh for the inversion of the ERT data. It included surface topography (the electrode positions were measured with differential GPS and the topography model was based on a linear interpolation between these points), the groundwater table, and the gravel - clay boundary at the base of the aquifer as delineated by Doetsch et al. (2012) using a well-defined reflector corresponding to the gravel-aquifer interface found throughout the inversion volume. No smoothing constraints were imposed across these interfaces during the inversion. Doetsch et al. (2012) found that including these interfaces, especially the gravel - clay boundary, was essential for obtaining meaningful resistivity models of the subsurface at this site. The ERT inversion model consisted of 197,117 cells with a maximum 0.8 m^3 cell volume. This mesh was extended and refined for the forward calculations, such that the forward mesh comprised 1,805,464 cells. Singularity removal was used for the forward calculations (Lowry et al., 1989; Blome et al., 2009)

by calculating the potential field (for a homogeneous earth) using a refined mesh around the electrodes.

By applying the finite-element modeling and inversion code BERT (Günther et al., 2006; www.resistivity.net) to data $\mathbf{d}_0$ collected prior to the tracer injection, we determined the static or baseline bulk resistivity model $\mathbf{m}_{bg}$. The starting model for this procedure had a homogeneous resistivity of 200 Ωm above the gravel‑clay boundary and 20 Ωm below; tests with a homogeneous 200 Ωm starting model gave very similar results. A horizontal anisotropy factor of two was used for the smoothness constraints to honor the layered structures imaged by the GPR survey. At each iteration, the inversion algorithm sought a model that minimized an objective function that comprised a data misfit term and a model structure term. The trade-off parameter λ describes the weight given to the model structure term. It was chosen to ensure that the bulk resistivity model obtained after a few iterations matched the data to the estimated error level. The resulting model contained the minimum structure capable of explaining the data. For the present data set, the inversion converged after 3 iterations using $\lambda = 50$, with two times stronger smoothing in the clay region (see Günther et al. (2006) and Günther and Rücker (2006) for details on the regularization used in BERT).

We suspect that the 60 − 300 Ωm range of resistivities of the unsaturated zone in the resulting baseline bulk resistivity model $\mathbf{m}_{bg}$ of Figure 2b are a function of varying water content and grain size distribution. The resistivities of the saturated gravel aquifer and clay aquitard are 200 − 350 and ~35 Ωm, respectively.

ERT time-lapse inversions

Whereas static (baseline) ERT inversion models reveal the electrical structure of the subsurface, time-lapse inversion models offer the possibility to observe the dynamics of a system by combining measurements at different times. The methodology of time-lapse ERT inversion is

an active field of research and novel approaches for including time-constraints are being developed and studied. We base our methodology on the well-studied ratio inversion scheme, introduced by Daily et al. (1992). We express a data set $\mathbf{d}_i$ recorded at time step i as:

$$\mathbf{d}_i = g(\mathbf{m}_i) + \boldsymbol{\varepsilon}_s + \boldsymbol{\varepsilon}_n + \boldsymbol{\varepsilon}_{ri}, \qquad (1)$$

where g is the forward operator that calculates the response of the model $\mathbf{m}_i$ with errors being distributed as static $\boldsymbol{\varepsilon}_s$, numerical $\boldsymbol{\varepsilon}_n$, and random $\boldsymbol{\varepsilon}_{ri}$ contributions. We assume $\boldsymbol{\varepsilon}_s$, which could include electrode positioning errors, coupling conditions or modeling errors, to be the same for all time-lapse data sets. Numerical errors $\boldsymbol{\varepsilon}_n$ caused by imperfections in the forward operator are similar for all resistivity models as long as the models do not change significantly during the time-lapse inversion process. Random observational errors $\boldsymbol{\varepsilon}_{ri}$ vary between time-lapse data sets. By using the same electrode installation for the entire duration of an experiment, it is usually reasonable to assume that $\left|\boldsymbol{\varepsilon}_s + \boldsymbol{\varepsilon}_n\right|_2 \gg \left|\boldsymbol{\varepsilon}_{ri}\right|_2$. Removing the effects of $\boldsymbol{\varepsilon}_s$ and $\boldsymbol{\varepsilon}_n$ from the input data is therefore desirable when inverting for resistivity changes.

Daily et al. (1992) introduced a scheme in which the ratios of the $\mathbf{d}_i$ and $\mathbf{d}_0$ data sets are inverted:

$$\tilde{\mathbf{d}}_i = \frac{\mathbf{d}_i}{\mathbf{d}_0} g(\mathbf{m}_{bg}). \qquad (2)$$

In the time-lapse inversions, we solve for updates to the baseline model $\mathbf{m}_{bg}$ using the logarithms of $\tilde{\mathbf{d}}_i$. This approach removes the effects of $\boldsymbol{\varepsilon}_s$ and $\boldsymbol{\varepsilon}_n$ and ensures reliable sensitivity patterns. For our experiment, we inverted the ratios of the 26 post-injection apparent resistivity data sets with the pre-injection data set using an isotropic value of $\lambda = 50$ and time-varying errors of $\left|\boldsymbol{\varepsilon}_{ri}\right|_2 = \left|\boldsymbol{\varepsilon}_s + \boldsymbol{\varepsilon}_n\right|_2 / 14$. Other error levels were tested, but 1/14 of the non-time-related errors provided the best compromise for a well resolved plume and limited inversion artifacts.

The results of the time-lapse inversions are distributions of 3D bulk resistivity change with respect to the baseline model. These distributions are closely linked to the tracer plume, because

the bulk resistivity distribution of the subsurface only changes in places where the resistivity of the water changes. The tracer plume is defined by the region where bulk resistivity changes ≥3%. Tests with plume thresholds of 2-5% showed that 3% is the best compromise between including significant inversion artifacts (2% threshold) and only defining the area around the center of mass (5% threshold).

Static and time-lapse ERT inversions are inherently limited in resolution, and parameter estimation (inversion) is non-unique (Friedel, 2003). To reduce the non-uniqueness, subsurface parameters are commonly assumed to vary smoothly. For time-lapse inversions, the subsurface model that explains the data with the minimum of changes with respect to the baseline model is thus preferred. As a consequence, the plume inferred from the ERT models is strongly smeared with reduced contrasts relative to the true subsurface situation.

ESTIMATING HYDROLOGICAL PARAMETERS FROM THE ERT TIME-LAPSE MODELS

Changes in groundwater electrical resistivity conductivity can be estimated from the ERT-determined bulk resistivity changes using Archie's Law (Archie, 1942). To do this, we neglect the contribution of surface conduction and assume a constant formation factor of 10. The fluid resistivity is then converted into salt concentration using the laboratory-derived calibration discussed in section "Salt tracer breakthrough". The amount of salt in each cell is then calculated from its salt concentration and volume assuming a porosity of 25%. Doetsch et al. (2010) estimated the formation factor and porosity at a neighboring aquifer and found variations about these values on the order of ±20-30%.

We calculate the zeroth, first, and second spatial plume moments from the time-lapse models using the 3% threshold-defined plumes and the salt concentration estimates. While moment inference from tomograms can give quantitative information about the hydrological system, the

estimated parameters depend rather strongly on the survey design and location of the plume in the model (Day-Lewis et al., 2007). The mass of the tracer or zeroth moment, is directly dependent on the threshold used for the tracer definition: a larger plume always has a larger mass. The center of mass of the tracer, which is the first moment normalized by the mass, is almost unaffected by the choice of the threshold (we chose a threshold of 3% change in resistivity, see above), because the center of mass is in most cases near the highest tracer concentrations and these decrease smoothly in all directions. The spatial variance, which is closely linked to the second moment, is again strongly influenced by the plume-definition threshold, because the size of the plume depends directly on it. In summary, the center of mass is well defined (Singha and Gorelick, 2005), but the mass and variance of the plume inferred from the smoothness-constrained ERT inversions should be interpreted with caution.

ERT-DETERMINED SALT TRACER PLUME TRACK

The 3D representation in Figure 5 shows the salt tracer plume 1 h after salt injection began and its subsequent evolution 6, 16, and 44 h later. The extent of the plume after 1h is affected by the 20 min tracer injection period and the resolution limitations of the ERT inversion (i.e., the plume is probably much more concentrated than shown). For the first 6 h, the plume spreads broadly in a general 25° direction relative to the x-axis (compare Figure 5a and b). From the moment analysis, we find that the center of mass moves with a velocity of 2×10^{-4} m/s and its front appears to move more than twice as fast at 5×10^{-4} m/s. After ~6 h, the main mass of the plume slows down while its front continues moving at a relatively high rate. A region of preferential flow along which the plume rapidly propagates is clearly seen at ~16 h in Figure 5c. In contrast to movements during the first 6 h, the plume moves parallel to the x-axis at these later times. Shortly after 16 h, the front of the plume has moved ~35 m and then leaves the area covered

16

by the electrode array. At times > 20 h, the plume appears to shrink. The decreasing size of the ERT-derived plume at later times (compare Figures 5d and 5c) is an effect of ERT experimental design, resolution, and detection limitations. While the true plume is continuously increasing in size, the remaining tracer mass in the well-resolved region of the aquifer is decreasing as the tracer gets more diluted and moves farther downstream into regions where ERT sensitivities are low. This means that reliable estimates of the tracer plume can only be obtained until ~16 h after tracer injection. The remains of the plume within the electrode array are found to move very slowly near the base of the aquifer at times > 40 h (Figure 5d).

The extracted cross-sections of relative resistivity change in Figure 6 highlight the density effects associated with the salt tracer. The plume's center moves downwards with time, especially between 1 and 6 h after tracer injection (compare Figure 6a and b). The effective mass recovery is 1.8 kg (10%) for the first time step, 1 h after injection, and increases to 4.5 kg (25%) at time step 11, 16 h after injection.

HYDROLOGICAL ASSESSMENT OF THE ERT RESULTS

Groundwater flow and transport model

Calibration of groundwater models is very difficult in river corridors with strong river – aquifer exchange and high hydraulic conductivities. Fortunately, the plume's center of mass under these conditions is a dependable source for calibration of hydraulic conductivity. We use a simplified 3D groundwater model with homogeneous parameter distributions (i.e., effective porosity, hydraulic conductivity, and dispersivities) and stationary boundary conditions. This latter assumption is supported by hydraulic-head time series acquired in multiple wells during the course of the experiment, which showed temporal changes in the hydraulic head field to be insignificant (see section "Salt tracer injection"). A homogeneous subsurface is assumed as a null hypothesis to

test which parts of the ERT models data can be explained by a homogeneous model and which parts require heterogeneity.

For the groundwater modeling, we use SEAWAT, which couples the MODFLOW and MT3DMS codes to simulate variable-density groundwater flow and transport in three dimensions (Langevin et al., 2008; Langevin, 2009). For our experiment, we employ a rectangular 3D model of $171 \times 79 \times 33$ cells that extends $70 \times 50 \times 6.6$ m. Grid discretization in the vertical direction is uniformly 0.2 m and that in the horizontal direction is 0.1 m around the injection well and increasing to 1 m away from the area of interest. The upper two model layers are either saturated or unsaturated during the simulation, whereas all other layers are always fully saturated.

Based on the results of previous hydrogeological investigations at the study site, the initial horizontal hydraulic conductivity was set to 3.1×10^{-3} m/s (Schneider et al., 2011) and the anisotropy (horizontal to vertical ratio) of hydraulic conductivity was taken to be 6.2 (Diem et al., 2010). Effective porosity was again set to 25%. Dispersivities were chosen to be 0.3, 0.03, and 0.003 m in the longitudinal, transverse, and vertical directions, respectively. These values were obtained by keeping typical ratios between dispersivities (Singha and Gorelick, 2005) and by varying the values so that the density effect in the simulations matched the ERT field results. Fixed head boundary conditions were applied at the upstream and downstream ends of the model to sustain the 1.43‰ hydraulic head gradient estimated from the measurements before the tracer experiment, whereas no flow boundaries were imposed on the other model sides.

The model was first run to steady state before simulating the salt injection and observation phases of the experiment. The flow equations were solved using a finite-difference scheme (preconditioned conjugate-gradient solver with head and flow convergence criteria of 10^{-7} m and 10^{-7} m^3/s, respectively) and the transport simulation used a finite volume approach (ULTIMATE conservative difference scheme (Leonard, 1991) for advective transport and a generalized conjugate gradient solver with a 10^{-6} convergence criterion for relative concentrations). Automatic

time stepping was employed for the combined flow and transport simulation. During manual model calibration, hydraulic conductivity was adjusted until the salt plume's center of mass in the hydrological simulations matched that of the ERT time-lapse model during the first 6 hours. The resulting calibrated horizontal hydraulic conductivity was 4×10^{-2} m/s, considerably higher than the 3.1×10^{-3} m/s value derived from multi-level slug tests (Schneider et al., 2011). While the modeled breakthrough using the calibrated hydraulic conductivity is consistent with the observed breakthrough in R072, the slug test derived hydraulic conductivities greatly overpredicts tracer arrival time.

Synthetic ERT experiment based on the groundwater transport modeling results

To test our time-lapse inversion scheme, establish its limitations, and assess the resolving capability of the ERT time-lapse models, we created synthetic data sets based on the calibrated groundwater model described in the section "Groundwater flow and transport model" and the ERT field layout and measurement schedule described in the section on "Data acquisition".

The bulk resistivity of the aquifer in the synthetic baseline model was taken to be homogeneous (i.e., neglecting surface conduction and assuming the formation factor to be homogeneous). Bulk resistivities within the unsaturated zone and clay aquitard were adopted from the inverted baseline model. The background electrical resistivity of the original groundwater was set to the 20 Ωm value measured just prior to the experiment, and the resistivities of the simulated tracer were estimated using the laboratory-derived relationship (section "Salt tracer breakthrough"). For the aquifer region of the model, the water resistivities were converted to bulk resistivities using Archie's Law with a formation factor of 10 (Doetsch et al., 2010). The bulk resistivity of the aquifer changed as the simulated plume propagated through the model, while the bulk resistivities of the unsaturated zone and clay layer did not vary.

Apparent resistivities calculated for the time-varying resistivity models using the forward component of the BERT code (Günther et al., 2006) were contaminated with Gaussian noise at the error level of the field data (i.e., a time-invariant error level $\left.|\boldsymbol{\varepsilon}_s + \boldsymbol{\varepsilon}_n|\right._2$ with a median of 3.8% and a time-varying error level of $\left.|\boldsymbol{\varepsilon}_{ri}|\right._2 = \left.|\boldsymbol{\varepsilon}_s + \boldsymbol{\varepsilon}_n|\right._2 \big/ 14$). The resulting synthetic data set were a reasonable match to the field data for the simulated ERT configurations and measurement times. The synthetic ERT data were then inverted in the same manner and with the same parameters as the field data, such that the resistivity models based on the synthetic and field data could be directly compared. We used the inversion models in the same way as the experimental results to define the tracer plume (i.e., defined by ≥3% change in bulk resistivity) and calculate the moments of the plume. Mass recovery for the synthetic study was much better than for the field experiment, with 14 - 15 kg (77 - 83%) of salt being imaged.

Comparison of the field-based and synthetic plumes

The tracer plume's center of mass (blue dots) and maximum horizontal extent (solid, dashed, and dotted lines) are presented in Figure 7 for the (a) time-lapse inversion results of the ERT field data, (b) the simulated groundwater transport model, and (c) the time-lapse inversion results of the synthetic ERT data. The plume derived from the time-lapse inversion of the field data is seen to disperse from the injection well over a wide azimuth until about 6 h, after which the front of the plume narrows and appears to flow along a relatively well-defined path (Figure 7a). By comparison, the plume in the simulated groundwater transport model is uniformly narrow along a linear flow direction (Figure 7b). The plume in the model derived from the synthetic ERT data appears to follow the same linear flow direction but with a much broader front (Figure 7c) with a width that is similar to the one inferred from the ERT field data (Figure 7a).

A comparison of the simulated groundwater plume (Figure 7b) with the plume estimated from the synthetic ERT data (Figure 7c) demonstrates the limited resolving power of the ERT method

using smoothness-constrained deterministic inversion in this environment. The ERT-defined plume is inherently much broader and therefore provides a relatively low resolution image of the simulated groundwater plume on which the synthetic ERT data are based. This behavior is quantified by showing the evolution of the second plume moments for the main flow direction (Figure 8a) and for the horizontal direction perpendicular to it (Figure 8b). It is clearly seen that the plume defined by inverting the synthetic ERT data is more dispersed than the simulated groundwater plume.

As a result of this limited resolution, to understand the differences between the plume derived from the time-lapse inversion of the ERT field data and the simulated groundwater plume, it is more meaningful to compare Figure 7a and 7c (they are affected by approximately the same resolution limitations) than Figure 7a and b. The shapes of the plumes in Figure 7a and c are similar for the first 6 h, but diverge at later times as the plume in Figure 7a narrows and starts to propagate along a well-defined path. Note how a portion of the tracer stays in the vicinity of the injection well for all times displayed in Figure 7a, whereas the entire tracer plume (as defined by the 3% resistivity threshold) has moved away from the injection well by ~9 h in Figure 7c. The effect of a fraction of the tracer staying close to the injection well is thus not captured by the groundwater model. The second moments derived from the field experiment shows consistently larger variances than those for the inversion of the synthetic data (Figure 8), indicating again that the spread of the actual plume is larger than in the groundwater model (Figure 7b). This is no surprise as the synthetic model is based on uniform properties, which is not the case for the true aquifer. As expected, the discrepancy along the flow direction grows after the first 6 hours.

By employing a homogeneous groundwater transport model to create the synthetic ERT data, the similarities between the plumes estimated from the field and synthetic data have helped identify apparent homogeneous transport behavior at the study site, whereas the differences have helped identify the influence of heterogeneity.

21

DISCUSSION

The ERT time-lapse images track the salt tracer plume for ~35 m. The 2×10^{-4} m/s velocity of the center of mass determined from the ERT time-lapse inversions agrees with the ~10^{-4} m/s value derived from natural variations in electrical resistivity time series (Vogt et al., 2010a). In contrast, our 4×10^{-2} m/s estimate of effective hydraulic conductivity is one order of magnitude higher than the 3.1×10^{-3} m/s geometric mean derived from slug tests (Schneider et al., 2011). We attribute this difference to the much larger observation scale of our study and the general tendency for the effective hydraulic conductivity to increase with observation scale (Neuman, 1990; Schulze-Makuch et al., 1999). Furthermore, the effective hydraulic conductivity might be closer to the larger arithmetic mean than the geometric mean, because the hydrogeology at the site is likely to be strongly influenced by interconnected high conductivity regions (Renard and de Marsily, 1997; Huggenberger et al., 1998). Note also, that the tracer injection will preferentially occur in the highest conductivity regions of the boreholes.

Considering the resolution limitations of the ERT models (see Figure 7), the arrival times and concentrations measured in the observation wells are consistent with the ERT time-lapse images. At observation well R072, which coincides with the path of the plume's center of mass (compare Figures 1b and 7a), high tracer concentrations are measured soon after injection begins. Tracer breakthrough occurs much later and the peak concentration is much lower at observation well R073, which is located 2.6 m to the side of the ERT-determined plume's center of mass and at the boundary of the plume obtained by the calibrated flow- and transport model (Figure 7b). It is clear that tracer transport is somewhat influenced by the 20 min of increased pressure in the injection well during the tracer injection which will initially spread the tracer in a radial pattern around the injection borehole. Unfortunately, the need to assure complete mixing in the injection well

precluded us from measuring the change of water level during the injection phase. This effect is included in the groundwater modeling, which predicts a hydraulic head change during the tracer injection of 0.1 cm. An indication of the resulting spreading of the plume is shown in Figure 7a after 1 h.

One finding of our study is the significant change of plume propagation direction (Figure 7a). It is unlikely that this change is due to changes in river level and resulting changes in hydraulic gradient within the aquifer. The hydraulic head time series in the observation wells would explain maximum variations of ±4° in the direction of the hydraulic gradient during our experiment, much smaller than the observed ~25° change in flow direction. We suggest that subsurface heterogeneities are responsible for the change in flow direction. The highly advective flow regime contributes to the effects of plume heterogeneity. For times >6 h, the plume front appears to move through a high hydraulic conductivity zone. From the ERT time-slices, it is difficult to determine the width or depth of this zone, but from Figure 6c it appears that the region of preferential flow was located in the lower part of the aquifer.

The long residence time of portions of salt tracer close to the injection well is noteworthy (Figures 5d and 6d). At times >40 h, the injection point is at the edge of the plume defined by the 3% change in resistivity. We conclude that the corresponding fraction of tracer is moving, but much slower than the tracer front. Indeed, the slow moving fraction of the tracer appears to be moving with a velocity ~20 times slower than the tracer front. Although this is a large spread of velocities, it is not uncommon for this type of gravel aquifer (Heinz et al., 2003). This observation is in accord with the long tail of the breakthrough curve measured in R072 (Figure 4). Many natural gradient tracer tests, such as natural gradient experiments at the Macrodispersion Experiment (MADE) site on the Columbus Air Force Base in Mississippi (e.g., Boggs and Adams, 1992), reveal tracer behavior that cannot be explained by classical stationary and Gaussian hydraulic conductivity fields (Boggs and Adams, 1992; Zheng, 2006). Several approaches have

been proposed to simulate the tracer transport observations at MADE, for example, by incorporating preferential flow paths (Zheng and Gorelick, 2003) or mass transfer between mobile and immobile domains (Harvey and Gorelick, 2000). The available data at our site do not allow us to favor one of these explanations.

The different mass recoveries inferred in the field (10-25%) and from a synthetic (~80%) model using ERT time-lapse images are the result of a number of factors. First, although we know the true error level of the synthetic data, it is difficult to estimate the time-lapse error ε_{ri} for the field data and the associated modeling. Second, our petrophysical model of a linear and uniform relationship between bulk resistivity and salt concentration (i.e., Archie's Law in combination with the laboratory-derived relationship between water resistivity and salt concentration) may not be strictly applicable at the study site (e.g., surface conductivity might be significant and both the porosity and the formation factor are spatially-varying properties). Third and foremost, the measured apparent resistivity values are, for a given tracer mass, more sensitive to large uniform features with small resistivity contrasts relative to background values than smaller irregular features with large resistivity contrasts. The upper Wiener bound of the effective electrical conductivity is the arithmetic mean of the averaging region (Renard and de Marsily, 1997) and irregularities in the conductivity distribution will always reduce this effective conductivity. The inversion process seeks the smoothest model that fits the data. Simulations based on the homogeneous groundwater transport model also produce smooth well-distributed low-concentration plumes, which means that the ERT inversion results for the synthetic example yields rather satisfactory mass recovery. The real tracer distribution is likely to be more heterogeneous at scales smaller than the resolution of the ERT time-lapse images (e.g., non-uniform tracer distribution in the pore space and in-between lithological units), which suggests that the ERT inversion can fit the data with a more uniformly distributed model containing less mass than in reality.

Heterogeneity in gravel deposits are known to be the source of significant hydraulic conductivity variations (see Beres et al., 1995; Huggenberger et al., 1998; Beres et al., 1999 and references therein). In analyzing 3D GPR and direct-push hydraulic data acquired at the MADE site, Dogan et al. (2011) found a non-Gaussian distribution of log hydraulic conductivity for the entire aquifer and much smaller hydraulic conductivity variations within GPR-defined zones. Likewise, the GPR-defined zones at the Thur field site (Doetsch et al., 2012) may represent zones of different hydraulic conductivity statistics. Applying direct-push hydraulic profiling to these zones with the goal of parameterizing groundwater models that are consistent with the ERT and breakthrough data would be a valuable extension of our work.

CONCLUSIONS

Transport of a saline tracer within a dynamic riparian groundwater system has been monitored using 3D surface ERT time-lapse inversion. A 500 l volume of saline solution (36 g/l salinity) was injected within a well that was screened throughout a 6-m-thick gravel aquifer with a natural hydraulic head gradient of 1.43‰. The overall shape of the salt tracer plume and its propagation direction and velocity were estimated. The tracer movement was roughly parallel to the flow of the river for the first 6 h, after which it changed direction by turning away from the river flow by 25°. The plume's front moved at a high $>5 \times 10^{-4}$ m/s velocity. After 16 h, the front had moved ~35 m, leaving the ERT-monitored region. The plume's center of mass traveled with a lower 2×10^{-4} m/s velocity. It was slightly influenced by its higher density relative to the natural groundwater. A significant tailing of the plume was also observed. In addition to demonstrating significant differences in groundwater flow velocity, our ERT time-lapse images suggested the existence of preferential flow paths, probably caused by localized higher permeability channels within the formation.

Our inability to follow the plume for more than 5 m using standard well-based hydrological observations serves to highlight the utility of 3D surface ERT time-lapse methods. Only two of the seven hydrological loggers located within ~30 m of the injection well registered a tracer signal. Moreover, the two breakthrough curves were difficult to interpret: one had a very fast response (tracer breakthrough ~50 min after the beginning of tracer injection) with high peak concentrations, whereas the other, located only 2.6 m from the first, had a slow response (tracer breakthrough after 20 h) and low peak concentrations. The solute transport appears to be controlled by complex subsurface structures typical of fluvial sedimentary environments. It cannot be resolved by a reasonable number of well observations alone.

We constructed a groundwater transport model to qualitatively assess the resolving capabilities of the ERT time-lapse images and determine if a homogeneous flow model could explain the ERT inversion results. We found that the observed ERT data could be adequately explained by a uniform 4×10^{-2} m/s hydraulic conductivity for the first ~6 hours after tracer injection. At later times, a homogeneous model provided an incomplete description

We recommend using 3D surface ERT for monitoring tracer experiments in dynamic shallow groundwater systems, because it i) allows 3D imaging of the tracer plume over time at larger scales than what is practical with crosshole ERT, iii) needs relatively little prior information about flow direction and velocity, and iv) is minimally invasive and comparatively inexpensive (e.g., no permanent installations are necessary). We stress that 3D coverage and 3D inversions are crucial for obtaining reliable estimates when studying 3D targets, such as a tracer plume. Two-dimensional inversions in such environments will always result in distorted inversion results that are case-specific and very difficult to quantify. One limitation of using ERT to investigate transport processes is the need to use high-salinity tracers that will induce significant density effects.

The types of smoothness-constrained ERT inversions that we present here do not provide detailed information about local spreading and mixing processes. Such processes are better captured using local hydrological monitoring data acquired in wells, the locations of which can be designed on the basis of the initial ERT monitoring experiments. For this case-study, we find that groundwater flow is more parallel with the river than assumed when installing the observation well transects, which explains the poor mass recovery in previous tracer tests. Furthermore, it appears that well transects oriented along a straight line are unlikely to follow flow paths for any longer distances, even when their orientation is optimal.

ACKNOWLEDGEMENTS

REFERENCES

Archie, G. E., 1942, The electrical resistivity log as an aid in determining some reservoir characteristics: Transactions of the American institute of Mining, Metallurgical and Petroleum Engineers, **146**, 54-62.

Bayer, P., P. Huggenberger, P. Renard, and A. Comunian, 2011, Three-dimensional high resolution fluvio-glacial aquifer analog: Part 1: Field study: Journal of Hydrology, **405**, 1-9, doi: 10.1016/J.Jhydrol.2011.03.038.

Bencala, K. E., 1984, Interactions of solutes and streambed sediment 2. A dynamic analysis of coupled hydrologic and chemical processes that determine solute transport: Water Resources Research, **20**, 1804-1814.

Beres, M., A. Green, P. Huggenberger, and H. Horstmeyer, 1995, Mapping the architecture of glaciofluvial sediments with 3-dimensional georadar: Geology, **23**, 1087-1090.

Beres, M., P. Huggenberger, A. G. Green, and H. Horstmeyer, 1999, Using two- and three-dimensional georadar methods to characterize glaciofluvial architecture: Sedimentary Geology, **129**, 1-24.

Binley, A., G. Cassiani, R. Middleton, and P. Winship, 2002, Vadose zone flow model parameterisation using cross-borehole radar and resistivity imaging: Journal of Hydrology, **267**, 147-159, doi: 10.1016/S0022-1694(02)00146-4.

Blome, M., H. R. Maurer, and K. Schmidt, 2009, Advances in three-dimensional geoelectric forward solver techniques: Geophysical Journal International, **176**, 740-752, doi: 10.1111/j.1365-246X.2008.04006.x.

Boggs, J. M., and E. E. Adams, 1992, Field study of dispersion in a heterogeneous aquifer: 4. Investigation of adsorption and sampling bias: Water Resources Research, **28**, 3325-3336, doi: 10.1029/92WR01759.

Butler, A. P., S. A. Mathias, A. J. Gallagher, D. W. Peach, and A. T. Williams, 2009, Analysis of flow processes in fractured chalk under pumped and ambient conditions (UK): Hydrogeology Journal, **17**, 1849-1858, doi: 10.1007/S10040-009-0477-4.

Cardenas, M. B., and M. S. Markowski, 2011, Geoelectrical imaging of hyporheic exchange and mixing of river water and groundwater in a large regulated river: Environmental Science & Technology, **45**, 1407-1411, doi: 10.1021/Es103438a.

Cardenas, M. B., J. L. Wilson, and V. A. Zlotnik, 2004, Impact of heterogeneity, bed forms, and stream curvature on subchannel hyporheic exchange: Water Resources Research, **40**, W08307, doi: 10.1029/2004WR003008.

Cassiani, G., V. Bruno, A. Villa, N. Fusi, and A. M. Binley, 2006, A saline trace test monitored via time-lapse surface electrical resistivity tomography: Journal of Applied Geophysics, **59**, 244-259, doi: 10.1016/j.jappgeo.2005.10.007.

Cirpka, O. A., M. N. Fienen, M. Hofer, E. Hoehn, A. Tessarini, R. Kipfer, and P. K. Kitanidis, 2007, Analyzing bank filtration by deconvoluting time series of electric conductivity: Ground Water, **45**, 318-328, doi: 10.1111/j.1745-6584.2006.00293.x.

Claerbout, J. F., and F. Muir, 1973, Robust modeling with erratic data: Geophysics, **38**, 826-844, doi: 10.1190/1.1440378.

Constantz, J., 2008, Heat as a tracer to determine streambed water exchanges: Water Resources Research, **44**, W00D10, doi: 10.1029/2008WR006996.

Daily, W., A. Ramirez, D. Labrecque, and J. Nitao, 1992, Electrical resistivity tomography of vadose water movement: Water Resources Research, **28**, 1429-1442, doi: 10.1029/91WR03087.

Day-Lewis, F. D., Y. Chen, and K. Singha, 2007, Moment inference from tomograms: Geophysical Research Letters, **34**, L22404, doi: 10.1029/2007gl031621.

Day-Lewis, F. D., J. W. Lane, Jr., J. M. Harris, and S. M. Gorelick, 2003, Time-lapse imaging of saline-tracer transport in fractured rock using difference-attenuation radar tomography: Water Resources Research, **39**, 1290, doi: 10.1029/2002WR001722.

Diem, S., T. Vogt, and E. Hoehn, 2010, Räumliche Charakterisierung der hydraulischen Leitfähigkeit in alluvialen Schotter-Grundwasserleitern: Ein Methodenvergleich: Grundwasser, **15**, 241-251, doi: 10.1007/s00767-010-0153-6.

Doetsch, J., N. Linde, I. Coscia, S. A. Greenhalgh, and A. G. Green, 2010, Zonation for 3D aquifer characterization based on joint inversions of multimethod crosshole geophysical data: Geophysics, **75**, G53-G64, doi: 10.1190/1.3496476.

Doetsch, J., N. Linde, M. Pessognelli, A. G. Green, and T. Günther, 2012, Constraining 3-D electrical resistance tomography with GPR reflection data for improved aquifer characterization: Journal of Applied Geophysics, **78**, 68-76, doi: 10.1016/j.jappgeo.2011.04.008.

Dogan, M., R. L. Van Dam, G. C. Bohling, J. J. Butler, Jr., and D. W. Hyndman, 2011, Hydrostratigraphic analysis of the MADE site with full-resolution GPR and direct-push hydraulic profiling: Geophysical Research Letters, **38**, L06405, doi: 10.1029/2010GL046439.

Dorn, C., N. Linde, T. Le Borgne, O. Bour, and L. Baron, 2011, Single-hole GPR reflection imaging of solute transport in a granitic aquifer: Geophysical Research Letters, **38**, L08401, doi: 10.1029/2011GL047152.

Friedel, S., 2003, Resolution, stability and efficiency of resistivity tomography estimated from a generalized inverse approach: Geophysical Journal International, **153**, 305-316.

Günther, T., and C. Rücker, 2006, A general approach for introducing information into inversion and examples from dc resistivity inversion: Presented at the 14th Annual European Meeting of Environmental and Engineering Geophysics, EAGE.

Günther, T., C. Rücker, and K. Spitzer, 2006, Three-dimensional modelling and inversion of dc resistivity data incorporating topography - II. Inversion: Geophysical Journal International, **166**, 506-517, doi: 10.1111/j.1365-246X.2006.03011.x.

Harvey, C. F., and S. M. Gorelick, 2000, Rate-limited mass transfer or macrodispersion: Which dominates plume evolution at the Macrodispersion Experiment (MADE) site?: Water Resources Research, **36**, 637-650.

Heinz, J., S. Kleineidam, G. Teutsch, and T. Aigner, 2003, Heterogeneity patterns of quaternary glaciofluvial gravel bodies (SW-Germany): Application to hydrogeology: Sedimentary Geology, **158**, 1-23, doi: 10.1016/S0037-0738(02)00239-7.

Hoehn, E., and O. A. Cirpka, 2006, Assessing residence times of hyporheic ground water in two alluvial flood plains of the Southern Alps using water temperature and tracers: Hydrology and Earth System Sciences, **10**, 553-563.

Huggenberger, P., E. Hoehn, R. Beschta, and W. Woessner, 1998, Abiotic aspects of channels and floodplains in riparian ecology: Freshwater Biology, **40**, 407-425.

Keery, J., A. Binley, N. Crook, and J. W. N. Smith, 2007, Temporal and spatial variability of groundwater-surface water fluxes: Development and application of an analytical method using temperature time series: Journal of Hydrology, **336**, 1-16, doi: 10.1016/J.Jhydrol.2006.12.003.

Kemna, A., B. Kulessa, and H. Vereecken, 2002, Imaging and characterisation of subsurface solute transport using electrical resistivity tomography (ERT) and equivalent transport models: Journal of Hydrology, **267**, 125-146, doi: 10.1016/s0022-1694(02)00145-2.

Kerrou, J., P. Renard, H. J. H. Franssen, and I. Lunati, 2008, Issues in characterizing heterogeneity and connectivity in non-multiGaussian media: Advances in Water Resources, **31**, 147-159, doi: 10.1016/J.Advwatres.2007.07.002.

Langevin, C. D., 2009, SEAWAT: A computer program for simulation of variable-density groundwater flow and multi-species solute and heat transport: U.S. Geological Survey, Fact Sheet 2009-3047.

Langevin, C. D., D. T. Thorne, Jr., A. M. Dausman, M. C. Sukip, and W. Guo, 2008, SEAWAT version 4: A computer program for simulation of multi-species solute and heat transport, USGS Techniques and Methods Book 6.

Leonard, B. P., 1991, The ULTIMATE conservative difference scheme applied to unsteady one-dimensional advection: Computer Methods in Applied Mechanics and Engineering, **88**, 17-74, doi: 10.1016/0045-7825(91)90232-u.

Lowry, T., M. B. Allen, and P. N. Shive, 1989, Singularity removal: A refinement of resistivity modeling techniques: Geophysics, **54**, 766-774, doi: 10.1190/1.1442704.

Monego, M., G. Cassiani, R. Deiana, M. Putti, G. Passadore, and L. Altissimo, 2010, A tracer test in a shallow heterogeneous aquifer monitored via time-lapse surface electrical resistivity tomography: Geophysics, **75**, WA61-WA73, doi: 10.1190/1.3474601.

Neuman, S. P., 1990, Universal scaling of hydraulic conductivities and dispersivities in geologic media: Water Resources Research, **26**, 1749-1758.

Park, S., 1998, Fluid migration in the vadose zone from 3-D inversion of resistivity monitoring data: Geophysics, **63**, 41-51.

Ramirez, A. L., and R. J. Lytle, 1986, Investigation of fracture flow paths using alterant geophysical tomography: International Journal of Rock Mechanics and Mining Sciences, **23**, 165-169.

RECORD, 2011, Assessment and modeling of coupled ecological and hydrological dynamics in the restored corridor of the river: Competence Center Environment and Sustainability, http://www.cces.ethz.ch/projects/nature/Record.

Renard, P., and G. de Marsily, 1997, Calculating equivalent permeability: A review: Advances in Water Resources, **20**, 253-278.

Schneider, P., T. Vogt, M. Schirmer, J. Doetsch, N. Linde, N. Pasquale, P. Perona, and O. A. Cirpka, 2011, Towards improved instrumentation for assessing river-groundwater interactions in a restored river corridor: Hydrology and Earth System Sciences, **15**, 2531-2549, doi: 10.5194/hess-15-2531-2011.

Schulze-Makuch, D., D. A. Carlson, D. S. Cherkauer, and P. Malik, 1999, Scale dependency of hydraulic conductivity in heterogeneous media: Ground Water, **37**, 904-919.

Singha, K., and S. M. Gorelick, 2005, Saline tracer visualized with three-dimensional electrical resistivity tomography: Field-scale spatial moment analysis: Water Resources Research, **41**, W05023, doi: 10.1029/2004wr003460.

Slater, L., A. M. Binley, W. Daily, and R. Johnson, 2000, Cross-hole electrical imaging of a controlled saline tracer injection: Journal of Applied Geophysics, **44**, 85-102, doi: 10.1016/S0926-9851(00)00002-1.

Stanford, J. A., and J. V. Ward, 1988, The hyporheic habitat of river ecosystems: Nature, **335**, 64-66.

Storey, R. G., K. W. F. Howard, and D. D. Williams, 2003, Factors controlling riffle-scale hyporheic exchange flows and their seasonal changes in a gaining stream: A three-

dimensional groundwater flow model: Water Resources Research, **39**, 1034, doi: 10.1029/2002wr001367.

Vogt, T., E. Hoehn, P. Schneider, A. Freund, M. Schirmer, and O. A. Cirpka, 2010a, Fluctuations of electrical conductivity as a natural tracer for bank filtration in a losing stream: Advances in Water Resources, **33**, 1296-1308, doi: 10.1016/j.advwatres.2010.02.007.

Vogt, T., P. Schneider, L. Hahn-Woernle, and O. A. Cirpka, 2010b, Estimation of seepage rates in a losing stream by means of fiber-optic high-resolution vertical temperature profiling: Journal of Hydrology, **380**, 154-164, doi: 10.1016/j.jhydrol.2009.10.033.

Ward, A. S., M. N. Gooseff, and K. Singha, 2010, Imaging hyporheic zone solute transport using electrical resistivity: Hydrological Processes, **24**, 948-953, doi: 10.1002/Hyp.7672.

Waxman, M. H., and E. C. Thomas, 1974, Electrical conductivities in shaly sands 1. Relation between hydrocarbon saturation and resistivity index 2. Temperature coefficient of electrical-conductivity: Journal of Petroleum Technology, **26**, 213-225.

Wilkinson, P. B., P. I. Meldrum, O. Kuras, J. E. Chambers, S. J. Holyoake, and R. D. Ogilvy, 2010, High-resolution electrical resistivity tomography monitoring of a tracer test in a confined aquifer: Journal of Applied Geophysics, **70**, 268-276, doi: 10.1016/j.jappgeo.2009.08.001.

Woessner, W. W., 2000, Stream and fluvial plain ground water interactions: Rescaling hydrogeologic thought: Ground Water, **38**, 423-429.

Zheng, C. M., 2006, Accounting for aquifer heterogeneity in solute transport modeling, *in* J. W. Delleur, ed., The Handbook of Groundwater Engineering, Second Edition, CRC Press, 1-18.

Zheng, C. M., and S. M. Gorelick, 2003, Analysis of solute transport in flow fields influenced by preferential flowpaths at the decimeter scale: Ground Water, **41**, 142-155, doi: 10.1111/j.1745-6584.2003.tb02578.x.

Zonge, K., J. Wynn, and S. Urquhart, 2005, Resistivity, induced polarization, and complex resistivity, *in* D. K. Butler, ed., Near Surface Geophysics: SEG, 265-300.
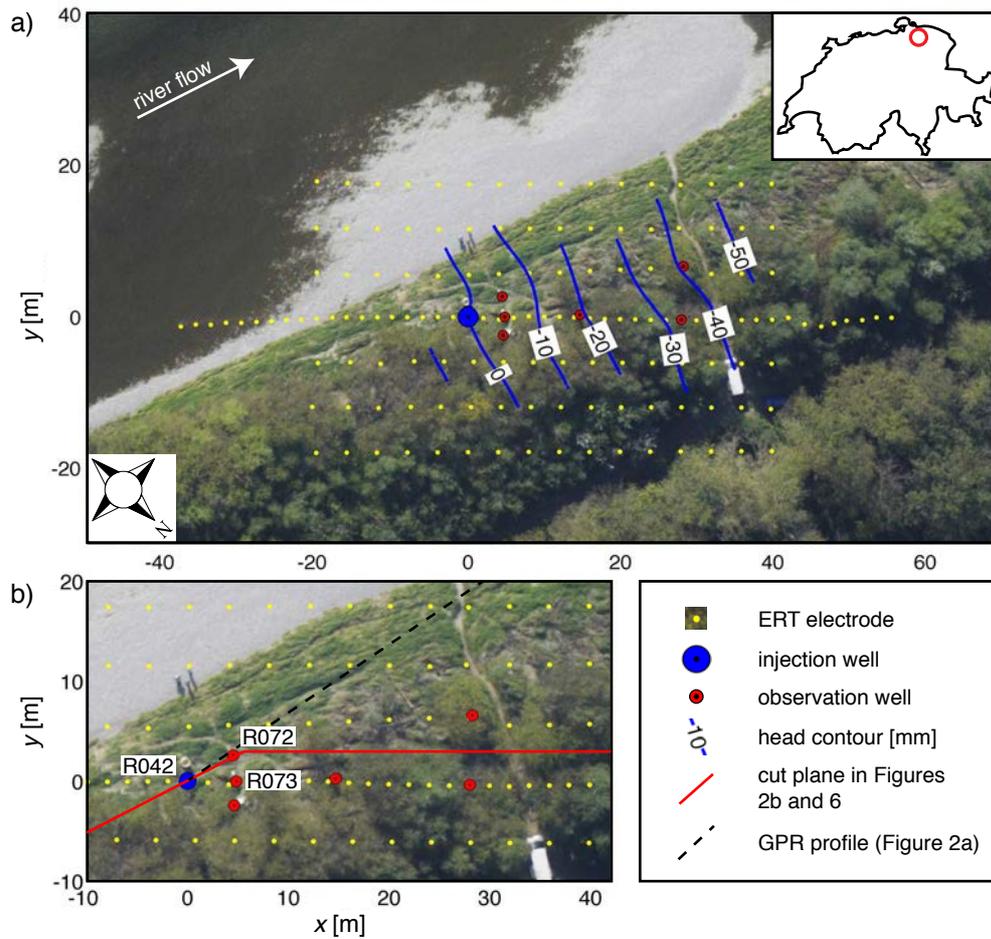
Figure 1. (a) Aerial Photograph of the Thur River bank (northeastern Switzerland, see inset) showing the injection (blue circle) and observation wells (red circles), ERT electrodes (yellow dots) and hydraulic head variation (in mm) with respect to the injection well. The head contours are interpolated from measurements in the injection well and six observation wells. (b) Magnified area of part of (a) showing the ERT model planes in Figures 2b and 6 (solid red lines) and GPR profile (dashed black line) in Figure 2a. The aerial photograph was taken at the time of the tracer test.
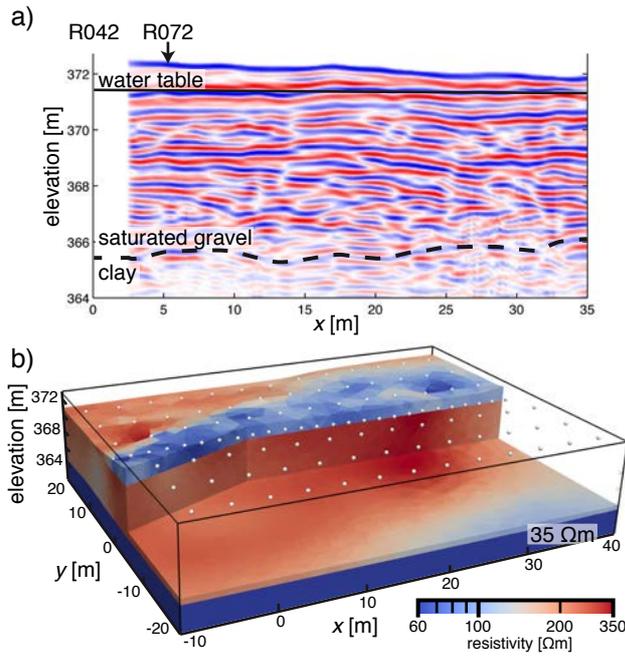
Figure 2. (a) GPR profile extending from the injection well in the direction of the initial tracer movement. The profile is extracted from the data of Doetsch et al. (2012). (b) Resistivity model obtained from ERT inversion of data acquired prior to tracer injection. This baseline model is used as the starting and reference model for the inversion. Dots at the surface are electrode positions. Resistivities in the unsaturated upper zone vary from $60 – 300$ Ωm (blue to red in the model); they are expected to be a function of water and clay content of the soil. The saturated gravel aquifer with resistivities of $200 – 350$ Ωm (uniformly red) is underlain by a clay aquitard with a resistivity of ~ 35 Ωm (dark blue).
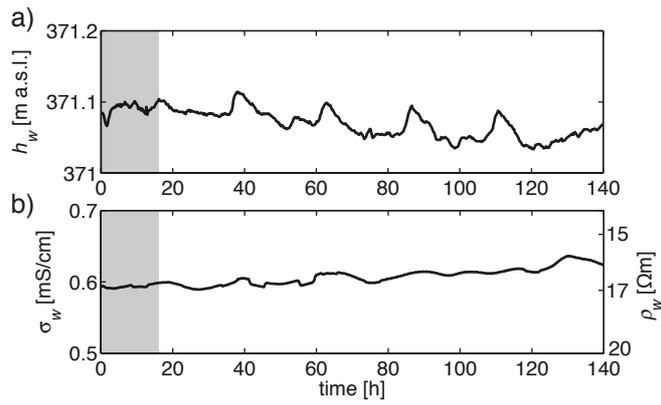
Figure 3. (a) River stage (water level) h_w and (b) electrical resistivity ρ_w and electrical

conductivity σ_w of the river water during the tracer test. Variations of h_w and ρ_w are minor during

the ERT experiment, especially during the first 16 h that are used for the interpretation (gray
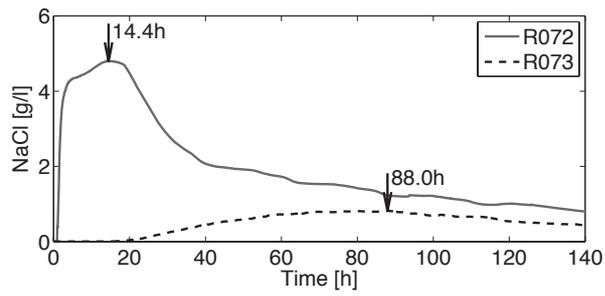
shaded area).

Figure 4. Salt tracer breakthrough curves measured at 366.9 m elevation (4.8 m below the groundwater table) in observation wells R072 and R073. The two observation wells are both located ~5 m from the injection well R042 (see Figure 1).
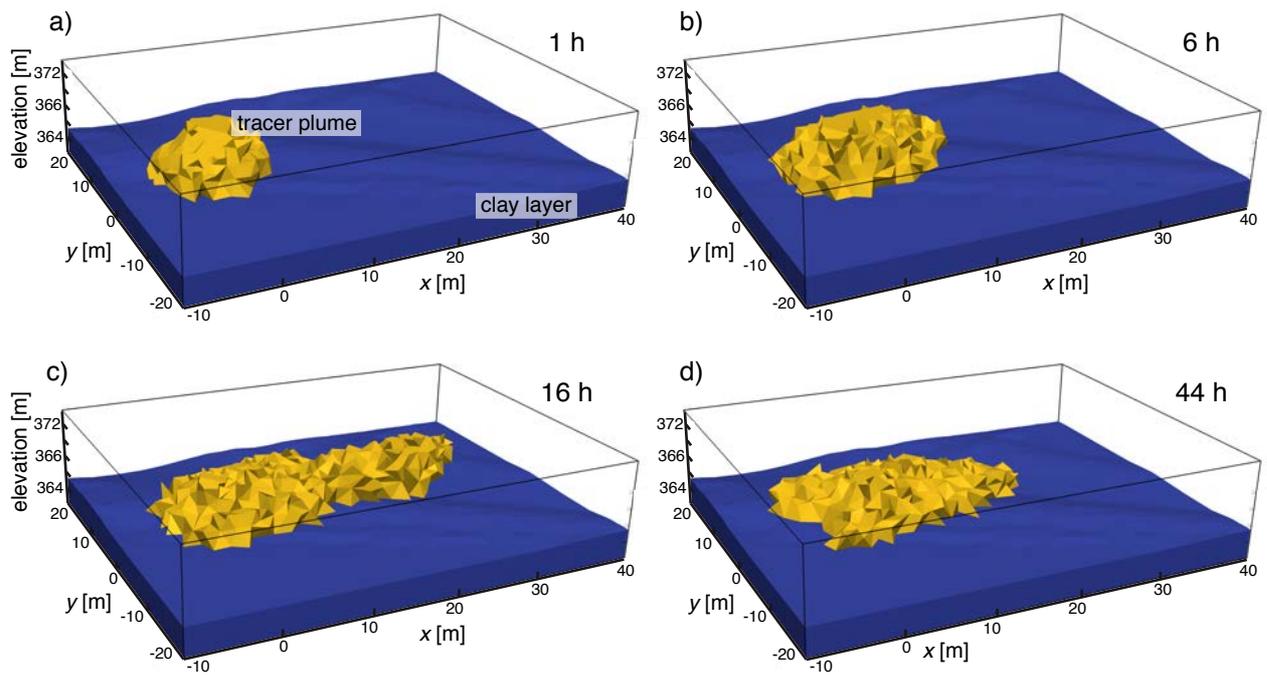
Figure 5. Tracer plume defined by a ≥3% decrease in bulk resistivity with respect to the baseline model (a) 1 h, (b) 6 h, (c) 16 h and (d) 44 h after the start of the tracer injection. See Figure 1 for the location relative to the river (the coordinate system is the same).
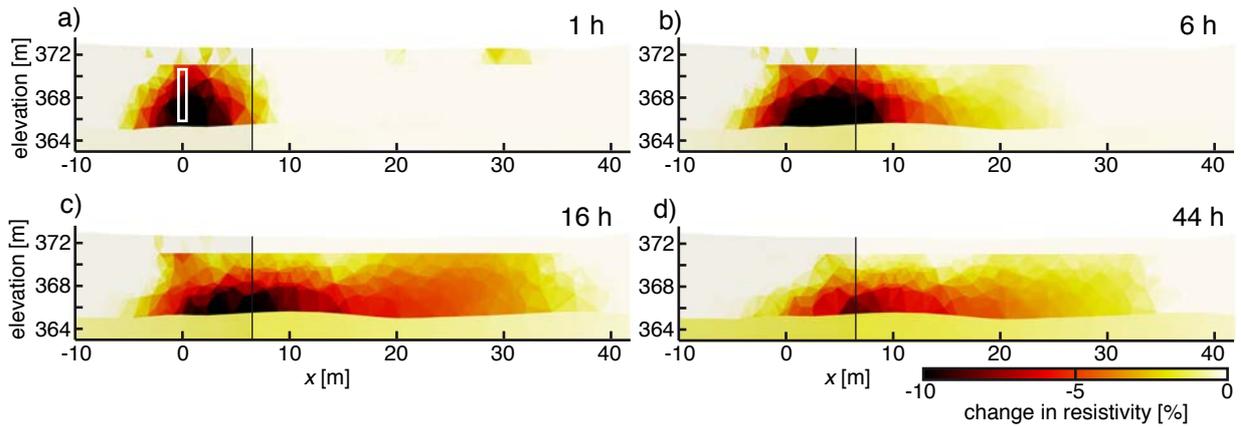
Figure 6. Cross sections of relative changes in resistivity (a) 1 h, (b) 6 h, (c) 16 h and (d) 44 h after start of the tracer injection. The change in resistivity is calculated with respect to the baseline model in Figure 2b. Position of the slice is shown in Figure 1b (red lines) and Figure 2b (face of the cut away). The white box in (a) marks the injection interval. Vertical black line marks the position of observation well R072. The coordinate system is the same as in Figure 1.
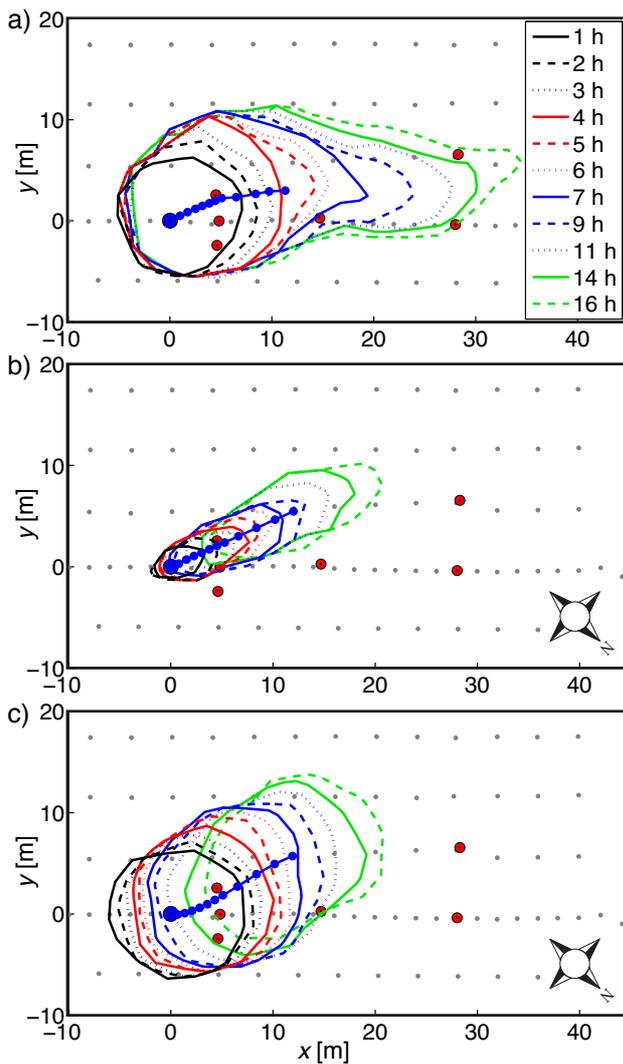
Figure 7. Plume outline from (a) ERT inversion of the field data, (b) groundwater modeling results and (c) ERT inversion of the synthetic data based on the groundwater simulation and petrophysical transformations. Lines correspond to the plume defined by a ≥3% decrease in resistivity for times 1 - 16 h (see legend) after the beginning of the tracer injection. Blue dots mark the center of mass. Note that the time intervals are not uniform. See Figure 1 for the location relative to the river (the coordinate system is the same).
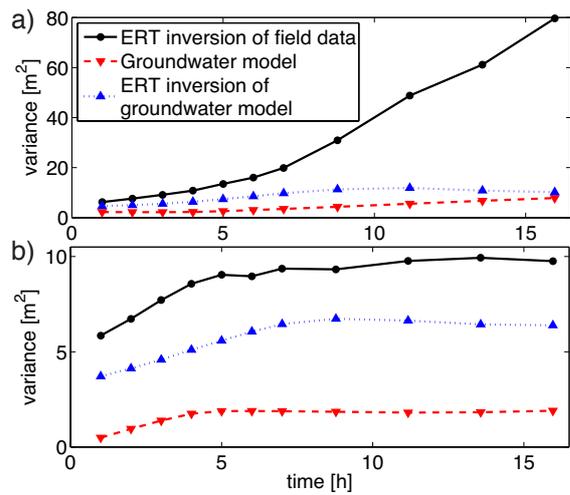
Figure 8. Development of the plume variances (a) in the flow direction and (b) perpendicular to it.